Prediction of resistance induced by surface complexity in lubricating layers: Application to superhydrophobic surfaces

Noura Bettaieb, Marco Castagna, Pierre-Yves Passaggia,
Azeddine Kourta, and Nicolas Mazellier ⬤*
University of Orléans, INSA-CVL, PRISME, EA 4229, 45072, Orléans, France

Superhydrophobic (SH) coatings have been demonstrated to reduce drag in various applications, though they have yet to be widely used or adopted due to practical issues. Various studies have demonstrated the prospect of reducing drag via SH surfaces both in turbulent and laminar flow regimes. However, the beneficial wall-slip effect produced may disappear depending on the surface geometry and flow conditions. The main mechanisms considered behind the decrease in performance are Marangoni-induced stresses and air/liquid interface deformation. In the present study, another mechanism is proposed to explain the loss of performances of SH surfaces in laminar flow regimes. Here we consider the flow of air inside the plastron and the associated momentum loss induced by roughness elements with different geometric characteristics. The effects of air motion within the plastron are coupled to the outer fluid with a homogenized boundary-condition approach. To this end, numerical simulations at the scale of the roughness elements were conducted as a function of the porosity and the tortuosity of the domain to determine the slip velocity at the air/liquid interface. The homogenized boundary condition is then implemented in a theoretical model for the outer flow to compute drag on SH spheres at low Re numbers. Experiments of laminar SH falling spheres indicate that high values of the tortuosity and low values of the porosity lead to a loss of performances when considering drag reduction. As anticipated, a three-dimensional printed sphere with low tortuosity and similar porosity demonstrated near-optimal drag reductions. A comparative study between the predicted values and experiments shows that the homogenized model is able to accurately predict the drag on SH surfaces for values of the porosity and tortuosity estimated from microscopy images of the SH textured surface.

I. INTRODUCTION

More than a century after the seminal work of Stokes [1], bluff-body drag and in particular its control remains an open question. Combined efforts from both theoretical fluid dynamics [2] and material sciences [3] demonstrated the potential of wall-slip-type surfaces towards drag reduction. Ideally, gas entrapment between the liquid and the solid induces a local slip condition that may favorably decrease drag via momentum transfer at the gas/liquid interface [4]. Gas lubrication can be practically achieved by using methods such as gas injection [5], the Leidenfrost effect [6], or combining surface texturing and chemical repellency [7]. The latter approach leads to the so-called superhydrophobic (SH) surfaces [8], which are at the core of this study.

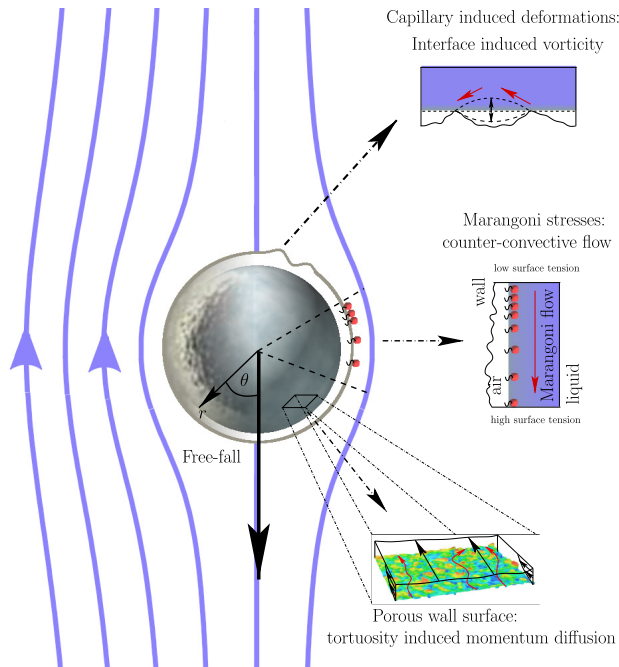
*nicolas.mazellier@univ-orleans.fr

FIG. 1. Schematics summarizing the possible mechanisms influencing the drag-reduction capabilities of SH coatings.

The SH property of the surface generates a high contact angle that repels water when in contact with the surface. Moreover, the presence of roughness elements on the surface results in cavities that entrap air and prevent water from infusing. These characteristics explain the potential of SH surfaces for reducing hydrodynamic drag. Precisely, since the surface retains a plastron, also referred to as a lubricating air layer, the friction resistance is decreased. The presence of an air layer changes the boundary condition at the wall from a zero-velocity condition to an interface between the outer liquid and the entrapped air.

Under these circumstances, the fluid experiences a sufficient slip on the surface that may reduce drag for both low and high Reynolds (Re) number flows [9]. Nevertheless, regarding flows over bluff-bodies, few available experimental studies [10–12] report mild-to-negligible drag reduction unlike predictions by theoretical and numerical works based on an ideal gas/liquid interface [9,13]. For instance, Ahmmed *et al.* [11] showed experimentally that SH surfaces may not contribute significantly to drag reduction in laminar flows. Precisely, they found that SH spheres presented higher drag compared to non-SH spheres. They concluded that although SH surfaces may reduce the friction drag, the form drag may increase due to the texture of the water repelling surfaces. As a result, they assumed that the increase in the form drag may outweigh the resultant SH effect, hence the overall drag could increase. Overall, these contradictions emphasize the need for improving the physical modeling of SH surfaces. One important aspect towards a better modeling would consist in identifying the mechanism behind performance degradation of SH surfaces.

Previous studies attempted to associate this mechanism considering various effects. Figure 1 illustrates some of the common effects that may contribute to degrading the performance of SH surfaces. Peaudecerf *et al.* [13] studied the Marangoni flow generated as a result of the surface tension gradient due to the buildup of contaminants on the air/liquid interface. They showed that surfactant-induced stresses can become significant, even for very low contaminants concentrations, potentially yielding a no-slip boundary condition over the flat air/liquid interface. These results were further extended by Song *et al.* [14], who demonstrated that Marangoni effects are dependent

on the roughness arrangement. Comparing closed cavities and continuous grooves, they showed that preventing surfactant from building up in the latter case induces a negligible surface tension gradient, restricting thereby the adverse effect of the Marangoni flow. Landel *et al.* [15] proposed a model to improve surfactant predictions for slip velocities. Their study was based on a model for two-dimensional, laminar, steady, and pressure-driven flow in a periodic SH channel. They showed how drag and slip depend on the characteristics of surfactant transport near the SH surface.

The deformation of the air/liquid interface may have an impact on the hydrodynamic performance of SH surfaces. Castagna *et al.* [16,17] investigated experimentally the role of air plastron deformation on the performance of falling SH spheres for different Re flow regimes. They demonstrated that the local distortion of the air pocket can trigger an early transition in the wake. More accurately, their results confirm that a slip boundary condition (BC) on the wall of the sphere may cause wake transition earlier than a no-slip BC causing the loss of the slippery effect. Additionally, they found that surface texture has an indispensable role on the value of the critical Re that triggers wake instabilities. Kim and Rothstein [18] conducted a set of experiments to study the effect of composite interface shape on laminar-drag reduction. Velocity and pressure drop measurements were conducted across a regularly distributed array of SH pillars. The shape of the contact surface between the outer liquid and air enclosed inside the SH-apple-core-shaped pillars was systematically altered from concave to convex. Results indicated that the intensity of the slip velocity depends strongly on the shape of the air/water interface. Further, the slip length was found to decrease as the interface grew from convex to flat to concave. Moreover, they highlighted that the maximum tangential velocity was found to be 45% of the average streamwise velocity. These conclusions were also presented in the work of Song *et al.* [14]. In addition to their investigation of the Marangoni effects, they observed that the flow over closed cavities is sensitive to the shape of the air/liquid interface. Convex air/liquid interfaces were found to maximize the slip velocity with respect to the concave counterpart.

Another mechanism (not portrayed in Fig. 1) may also explain the decrease in SH-surface efficiency. The fragmentation of the pocket air into the surrounding liquid can result in a decrease of the effective slip length. Govardhan *et al.* [19] studied experimentally the flow across randomly textured hydrophobic surfaces with water as the working fluid. Direct visualizations of enclosed air pockets were performed for the purpose of understanding the time-dependent slip length in stationary flows. The visualization of the bright spots at the composite interface, which were based on the principle of total internal reflection of light, confirmed the decrease of the number of air pockets with time. Henceforth, the timescale for the decrease in the slip length would eventually control the time for which the SH surface remains efficient. Another study by Ling *et al.* [20] studied the impact of gas diffusion on the volume of the plastron. Factors such as the flow regime and the ambient pressure were considered. Experiments demonstrated that the pressure increase resulted in a migration of the interface into the groove, together with a high advancing contact angle. In contrast, a pressure decrease caused an upward migration of the contact surface resulting in a convex interface. It was also found that the diffusion rate increases with increasing Re.

Previous works confirm that the features of the plastron have an impact on the performance of SH surfaces. In other words, the air flow inside the plastron may have a key role in determining the efficiency of the water-repellent surface. This effect has been studied numerically by Gruncell *et al.* [9], where baffles, used to model roughness elements, resulted in a flow with a recirculation region, unlike the case of a perfect plastron. Consequently, the drag-reduction effect decreased since the slip velocity around the edges of the baffles (same behavior for real roughness elements) also decreased. Furthermore, an increase in the solid fraction (SF) of the textured surface reduces the performance of SH surfaces. To be exact, the decrease in the porosity of the domain, caused by the increase of SF, may generate an increase in the relative blockage, hence a drag increase. Indeed, the porosity of the plastron has a great impact on the performance of SH surfaces and should therefore be considered when quantifying the slippage effect of SH surfaces. Regarding the quantification of the superlubricating effect, previous studies already proposed scaling laws that depend on the generic geometric characteristics of the surface. Ybert *et al.* [21] proposed expressions

that can be used to determine frictional properties of SH surfaces. The solid fraction of the interface and the roughness lengthscale, among others, were found to play a major role.

In this work, we take another step at modeling the role of textured SH surfaces in modifying friction drag. In particular, an effect responsible for reducing the efficiency of SH surfaces is introduced. Combining the air flow features inside the plastron in addition to the surface texture characteristics, we show that the increase in skin friction can be related to the air movement between the roughness elements inside the air layer. Specifically, we propose a simple model for the interaction of the moving air within roughness elements with complex patterns. The motion in the air layer is found to induce significant friction, capable of affecting slip at the air/liquid interface. It is quite obvious that the porosity of the domain has a key role in determining the intensity of the drag. A larger domain porosity yields a larger interface between the liquid and the gas layer, hence a larger slip velocity. On the contrary, it is not pronounced that the path length the air is forced to follow may have an impact on the amount of liquid slippage. It is worth noting that the air flow path, also referred to as the tortuosity, has not been considered in any of the previous cited research. Figure 1 illustrates the idea that air pockets are encapsulated between roughness elements, similarly to a porous medium. In that case, a porous medium approach can be used to model the motion of air through the surface texture. In other words, instead of solving the fine scale details at the interface level, one can implement a single boundary condition, capable of describing the slip velocity of the fluid considering only geometric features such as the tortuosity and the porosity.

A simple yet effective way to ascribe a complex BC can be performed using homogenization approaches. For instance, Naqvi and Bottaro [22] explored the interfacial conditions between a free fluid and a porous medium based on a Beavers-Joseph-Saffman condition. The study considered an isotropic medium approach through which model coefficients were derived for two- and three-dimensional-type textures. The proposed condition was verified through feature-resolving simulations up to higher Reynolds number (Re = 500) compared to those valid for the classical theory. In another study, Bottaro and Naqvi [23] proposed two different approaches to develop effective boundary conditions that model flow over walls with regularly distributed microstructures. The method was based on harmonizing the solution of the outer flow dependent on macroscopic variables to that of the inner flow that depends on large- and small-scale variables. The effect of surface texture is transferred to the outer flow through the inner equations at the interface level. The same concept is considered in this study in order to determine a homogenized BC that determines slip velocities for a SH material, in terms of the porosity and tortuosity of the medium. In this case, the effect of the roughness elements arrangement on the dynamics of the outer flow can be captured through the homogenized slip velocity expressions. A relationship between drag in creeping flow and slip velocity is needed thereafter.

The paper is organized as follows: In Sec. II, Stokes' flow around a sphere with an imposed slip velocity at the wall is first proposed, followed by a homogenization of the boundary condition at the air/liquid interface. The BC at the composite interface is expressed in terms of the geometric characteristics of the surface (porosity and tortuosity) which are determined via numerical investigations. In Sec. III, the falling experiments of SH spheres with random distributed roughness elements are introduced. The performance of spheres with different coatings is first discussed in Sec. IV. A comparison of the predicted drag using the proposed model and that obtained from experiments is performed. In light of the obtained results, an additional SH sphere with structured roughness elements is manufactured and tested both experimentally and theoretically. Conclusions are drawn in Sec. V.

II. STOKES' FLOW AROUND A SPHERE WITH PARTIAL SLIP

The homogenization procedure begins with solving the laminar flow around a sphere with a slip velocity at the surface of the sphere. The values of the slip velocity are determined by the characteristics of the SH surface in Sec. II B, and drag is used as a global measure for the validation with experiments.

A. Creeping flow around a SH sphere

In the present model, the tangential component of the velocity is defined as a function of the slip velocity rather than the slip length (see [24] for a recent work). It is worth noting that the slip length tends to infinity when reaching full-slip conditions while the slip-velocity remains finite. In addition, the present model allows for framing results beyond the full-slip case, which could prove relevant for mechanisms such as the Leidenfrost effect [6] or air injection [25].

The flow around a slipping sphere is solved analytically using Stokes' approach based on a stream function formulation. The two components of the velocity are defined as

$$u_r = \frac{1}{r^2 \sin\theta} \frac{\partial\psi}{\partial\theta}, \quad u_\theta = -\frac{1}{r\sin\theta}\frac{\partial\psi}{\partial r}, \tag{1}$$

where the polar velocity u_φ is assumed to be null. This streamfunction is a solution of the biharmonic equation:

$$\nabla^2(\nabla^2\psi) = 0, \tag{2}$$

where the Laplacian ∇^2 in spherical coordinates reads

$$\nabla^2 = \frac{\partial^2}{\partial r^2} + \frac{1}{r^2\sin\theta}\frac{\partial}{\partial\theta}\left[\sin\theta\frac{\partial}{\partial\theta}\right].$$

The boundary conditions in the present problem are as follows:

(i) A no-penetration condition at $r = R$:

$$u_r(r = R, \theta) = 0 \Rightarrow \frac{1}{r^2\sin\theta}\frac{\partial\psi}{\partial\theta} = 0 \ \forall\,\theta. \tag{3}$$

(ii) A slip condition at $r = R$, that is, $u_\theta(r = R, \theta) = U_{\text{slip}}f(\theta)$, where U_{slip} is the slip velocity and $f(\theta) = \exp(im\theta)$ is chosen as the azimuthal harmonic θ (spherical harmonic). Based on the biharmonic equation for the stream function, $f(\theta)$ only admits a restricted number of solutions, that is, $\nabla^2 f(\theta) = \omega f(\theta)$. The solution that induces the least amount of friction (i.e., the largest ω) is the first eigenvalue $m = 1$, which also provides the least amount of dissipation/the smallest drag coefficient. Note that $m = 0$ recovers the no-slip condition. In that case, the tangential velocity on the wall of the sphere reads

$$u_\theta(r = R, \theta) = -U_{\text{slip}}\sin\theta \Rightarrow -\frac{1}{r\sin\theta}\frac{\partial\psi}{\partial r} = -U_{\text{slip}}\sin\theta \ \forall\,\theta. \tag{4}$$

(iii) A far-field condition $r \rightarrow \infty$:

$$\psi = \frac{U_\infty r^2}{2}\sin^2\theta, \tag{5}$$

where U_∞ denotes the free-stream velocity.

The general solution of the stream function when considering a slip velocity condition therefore reads

$$\psi(r, \theta) = \frac{U_\infty r^2}{2}\sin^2\theta\left[1 - \frac{3}{2}\left(\frac{R}{r}\right)\left(\frac{3U_\infty - 2U_{\text{slip}}}{3U_\infty}\right) + \frac{1}{2}\left(\frac{R}{r}\right)^3\left(\frac{U_\infty - 2U_{\text{slip}}}{U_\infty}\right)\right]. \tag{6}$$

The details of the derivation of Eq. (6) are presented in detail in the Supplemental Material [26]. The radial and tangential velocity, therefore, read

$$u_r(r, \theta) = \frac{U_\infty}{2}\cos\theta\left[2 - 3\left(\frac{R}{r}\right)\left(\frac{3U_\infty - 2U_{\text{slip}}}{3U_\infty}\right) + \left(\frac{R}{r}\right)^3\left(\frac{U_\infty - 2U_{\text{slip}}}{U_\infty}\right)\right], \tag{7}$$

$$u_\theta(r, \theta) = \frac{U_\infty}{4}\sin\theta\left[3\left(\frac{R}{r}\right)\left(\frac{3U_\infty - 2U_{\text{slip}}}{3U_\infty}\right) + \left(\frac{R}{r}\right)^3\left(\frac{U_\infty - 2U_{\text{slip}}}{U_\infty}\right) - 4\right]. \tag{8}$$

Considering the above expressions, pressure and viscous drag can be expressed as follows:
Viscous drag from shear stresses,

$$F_{\text{skin}} = 4\pi\mu_l RU_\infty \left(\frac{U_\infty - 2U_{\text{slip}}}{U_\infty} \right). \tag{9}$$

Viscous drag from normal stresses,

$$F_{\text{normal}} = \tfrac{16}{3}\pi\mu_l RU_{\text{slip}}. \tag{10}$$

Pressure drag,

$$F_{\text{pressure}} = 2\pi\mu_l RU_\infty \left(\frac{3U_\infty - 2U_{\text{slip}}}{3U_\infty} \right). \tag{11}$$

Consequently, the total drag force applied on a SH sphere can be formulated in terms of the slip velocity as follows:

$$F_{\text{total}}^{\text{SH}} = 6\pi\mu_l RU_\infty \left[1 - \frac{2}{3}\frac{U_{\text{slip}}}{U_\infty} \right], \tag{12}$$

which leads to the following expression for the drag coefficient:

$$C_D^{\text{SH}} = \frac{24}{\text{Re}_\infty} \left[1 - \frac{2}{3}\frac{U_{\text{slip}}}{U_\infty} \right] = \frac{24}{\text{Re}_\infty}\xi_{\text{SH}}, \tag{13}$$

where ξ_{SH} denotes the drag correction factor.

For the free-slip surface the tangential shear stress is absent, hence the liquid slips with a velocity $U_{\text{slip}} = U_\infty/2$. As a result, the theoretical drag would be

$$C_D^{\text{SH}} = \frac{16}{\text{Re}_\infty}. \tag{14}$$

The development of the theoretical model and its validation using numerical simulations are presented in detail in the Supplemental Material [26].

For realistic surfaces, where roughness elements exist, the slip velocity can hardly reach the full slip case given in Eq. (14) since the plastron may not entirely cover the surface of the sphere. Under these conditions, U_{slip} has to be expressed in terms of the characteristics of the surface, which is assumed here to be a porous medium. Since a porous medium is customarily characterized by its porosity, the latter would be an obvious key parameter in investigating the features of the air flow. The medium can also be characterized by other properties, e.g., permeability, tensile strength, electrical conductivity, and tortuosity. These properties play vital roles in specifying the morphology of porous media. Among these properties, the tortuosity of the domain constitutes a key criterion in various scientific fields. This parameter is closely related to the transport behavior of fluid permeation, heat transfer, electrical conduction, and molecular diffusion. Consequently, this feature will impact the effective diffusivity and formation resistivity factor [27]. In other words, tortuosity is responsible for predicting the transport properties of a porous medium. This highlights the importance of these parameters and further confirms their selection as control parameters to be included in the present model.

In what follows, the slip velocity is determined as a function of the geometric features of a SH surface where we consider the flow inside a textured surface. The expression should involve two parameters: (i) the porosity and (ii) the tortuosity of the surface. The aim is to calculate the mean slip velocity U_{slip} and determine whether it can be approximated as scaling laws. We propose an analogy with the flow across microchannels where the tortuosity and the porosity can be controlled independently. The resulting homogenized slip is subsequently used in Eq. (13) to estimate drag.
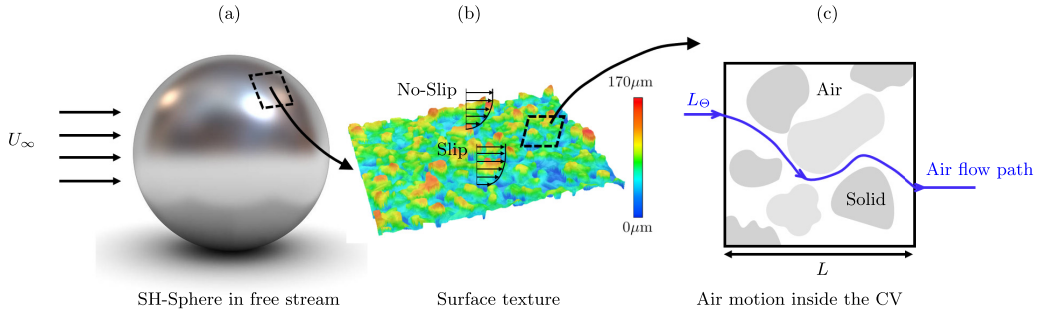
FIG. 2. Illustration of the air flow through roughness elements of (a) a SH sphere. (b) Confocal microscopy analysis of a portion (1.5×1.0 mm^2) from a flat plate covered by a fine grain SH coating. The color scale (blue-to-red) indicates the surface roughness height (0–170 μm). Notice the random spatial distribution of the powder particles. (c) Illustration of the gas pathline through a sample of random roughness elements.

B. Homogenized boundary condition

In the current study, it is assumed that the Reynolds number characterizing the flow inside the plastron may be different from that of the outer flow. In other words, the outer flow regime can be considered at finite Reynolds numbers while the inner flow (flow inside the plastron) may remain in a creeping-type regime. As a consequence, the linearity of Stokes' regime holds, and a linear superposition between the flow driven by a pressure gradient inside the grooves and a shear-driven flow imposed on the plastron interface can be sought as a solution for the flow inside the plastron.

As depicted in Fig. 2, the interfacial boundary condition alternates between no-slip and slip condition because of the random positioning of roughness elements. As a result, the mean slip velocity varies under the effect of porosity. A closer look at the movement of air between the roughness elements shows the tortuous path the air may follow, which can also alter slip at the wall. The air flow path is referred to as the tortuosity Θ of the control volume (CV). It is defined as the ratio of the actual path followed by the air (L_Θ) and length of the control volume (L). The arrangement of roughness elements from Fig. 2 yields a tortuosity $\Theta > 1$, whereas it is anticipated that if the surface is composed of structured elements, pillars for instance, air will experience less resistance. Thereby, flow paths will be relatively straight, $\Theta \approx 1$.

Figure 3 further illustrates how the local slip velocity varies for the case of randomly distributed roughness elements. More precisely, slip can be highly intermittent since the air void is different from one air pocket to another. The homogenization approach hence consists in finding an expression for the mean slip velocity that accounts for the geometric characteristics of the plastron and the motion of air inside it.
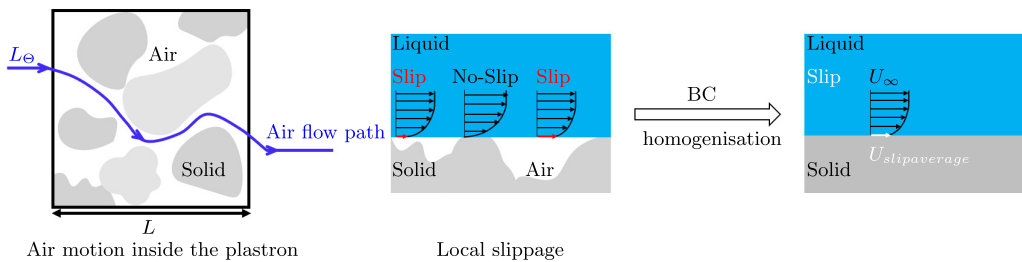

FIG. 3. Homogenization of the boundary condition at the air/liquid interface in terms of the geometric characteristics of the SH surface.
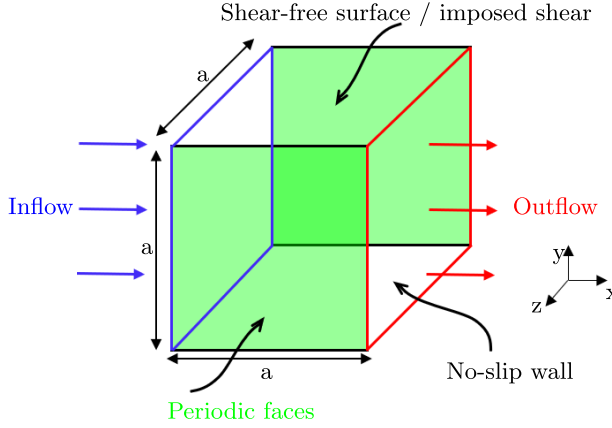
FIG. 4. Illustration of the computational domain.

To explore the role of surface texture, slip velocity was computed numerically for different cases where the geometry of the domain was varied. Different types of channels may provide access to a wide range of values for both tortuosity and porosity, namely wave-type channels, sawtooth channels, and sinuous channels. In the present study, sinuous channels were considered due to their simplicity. Sinuous channels provide the possibility of varying the porosity and the tortuosity independently in addition to efficient domain meshing. Figure 5 depicts the geometry used to force the fluid to follow a sinusoidal path. It is clearly visible that the air flow path is longer than the length of the CV.

Considering the above described geometry, numerical simulations of air motion inside the plastron were performed. The homogenization approach was derived from a study based on the classical concept of a control volume (see Fig. 4). The air flow inside the CV was considered incompressible, laminar, and steady. The continuity and momentum equations were normalized considering U_∞ and the CV height a. The obtained reduced formulations are hence the following:

$$\frac{\partial U_i}{\partial X_i} = 0, \quad U_j \frac{\partial U_i}{\partial X_j} = -\frac{\partial P}{\partial X_i} + \frac{1}{\mathrm{Re}} \frac{\partial^2 U_i}{\partial X_j^2}. \tag{15}$$

The term P represents the normalized pressure, whereas Re is defined as $\mathrm{Re} = \rho_{\mathrm{air}} U_\infty a / \mu_{\mathrm{air}}$. ρ_{air} and μ_{air} are the density and dynamic viscosity of air, respectively. The analysis is based on an idealized SH surface in the Fakir state subject to a steady laminar flow. Under these assumptions, the liquid lies on the upper surface of the roughness elements. Accordingly, the interface between liquid and gas is considered flat, which results in a flat composite interface. Further details on the CFD model are presented in the Supplemental Material [26].

Different boundary conditions are required to account for the pressure-driven flow (PDF) and the shear-driven flow (SDF). For instance, in the case of PDF, regions connecting liquid and gas were set as shear-free surfaces, whereas the contact between roughness elements and the liquid (solid regions of the CV) were set as no-slip walls (see Fig. 4). The lower surface and the walls of the channel were considered as no-slip walls, and the rest of the CV surfaces were considered as periodic boundaries with a pressure gradient between the inflow and outflow boundaries. The air flow velocity on the interface is equal to the liquid slip velocity. The continuity is the result of assuming that the interface is not deforming. Using the considered boundary conditions, the velocity profile inside the CV is the well-known Poiseuille flow whose solution reads $U(Y) = \mathrm{Re}(\partial P / \partial X)(y^2/2 - y)$. The nondimensional pressure gradient in this case is taken as $\partial P/\partial X = -2/\mathrm{Re}$. Meanwhile, the boundary condition for the SDF differs from the PDF type in defining the regions connecting the gas and the liquid and the in-and-out flow boundaries. A specified shear in the direction of the flow is
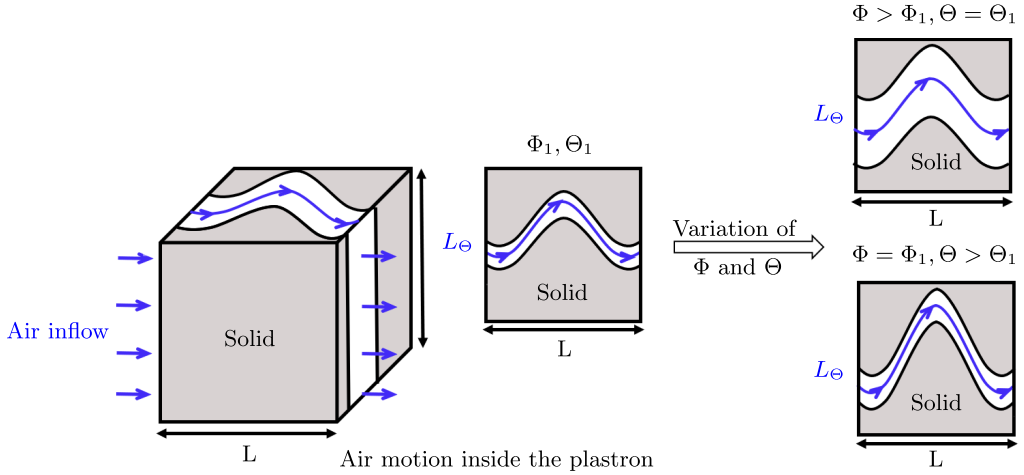
FIG. 5. Schematic of a porous medium model over a control volume (width L and height h) inside the air layer on the surface of a SH sphere. Gray regions are occupied by the solid while white regions are occupied by the air.

imposed on the upper surface with a zero-pressure gradient between inflow and outflow boundaries. The resulting flow is a simple Couette-type flow. For each type of flow, the air motion within the channels was investigated for two different scenarios. In each case, one of the two geometric characteristics was varied while the other was kept constant. For instance, given a defined geometric tortuosity Θ_1, simulations were performed for different values of the porosity Φ. To compute the fraction of air occupied in the CV, that is, the porosity Φ, the following expression is used:

$$\Phi = \frac{A_g}{A_g + A_s}, \tag{16}$$

where A_g and A_s are the gas and solid volumes, respectively. The air flow path was computed using the geometric definition of the tortuosity. In the case of sinuous channels, L_Θ is equal to the length of the channel walls. Figure 5 further indicates how Φ and Θ are varied independently. Consider a first configuration where the porosity and the tortuosity are Φ_1 and Θ_1, respectively. The porosity of the CV is increased ($\Phi > \Phi_1$), at a constant Θ, by increasing the distance between the walls of the channel. A tortuosity increase ($\Theta > \Theta_1$) was achieved by increasing the amplitude of the sinuous shape of the channel. Note that the finite CV size imposed a limited range of variation for both Φ and Θ. The chosen values for Θ ranged between $\Theta = 1.024$ and 1.463, whereas the porosity Φ in the CV varied within 5–45%. For each simulation, the normalized slip velocity $U^\star_{\mathrm{slip}} = U_{\mathrm{slip}}/U_\infty$ is calculated as the spatial mean value of the velocity on the upper surface of the CV.

For the PDF, the variation of $U^\star_{\mathrm{slip}}$ with respect to the geometric characteristics of the CV is shown in Fig. 6. At a constant value of Θ, Fig. 6(a) shows that the normalized slip velocity increases with increasing Φ. This is expected since a larger porosity provides a larger slip area between the liquid and the gas. However, a deeper look at Fig. 6(a) reveals that the increase in tortuosity results in a remarkable decrease of the slip velocity. In fact, for L_Θ less than $1.2L$, the slip velocity is approximately 40% less compared to the smallest values of the investigated tortuosity. Figure 6(c) shows the effect of the tortuosity on the mean slip velocity for constant values of Φ. A similar behavior is observed and slip is favored when a higher percentage of void and lower values of L_Θ are considered. Figures 6(b) and 6(d) illustrate the variation of the scaled slip velocity defined as $U^\star_{\mathrm{slip}\text{-}\Theta} = U^\star_{\mathrm{slip}}/U^\star_{\mathrm{slip}}(\Phi = 0.45)$ and $U^\star_{\mathrm{slip}\text{-}\Phi} = U^\star_{\mathrm{slip}}/U^\star_{\mathrm{slip}}(\Theta = 1.024)$ for constant tortuosity and constant porosity simulations, respectively. From Fig. 6(d), more than 70% of the slip velocity is
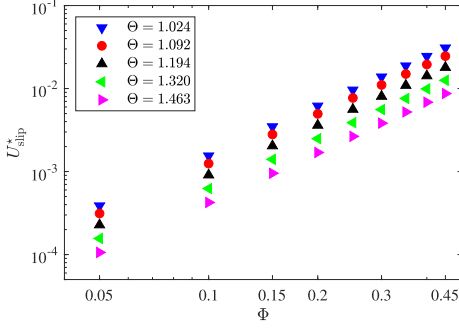
(a) Constant tortuosity, $U^\star_{\text{slip}} = U_{\text{slip}}/U_\infty$
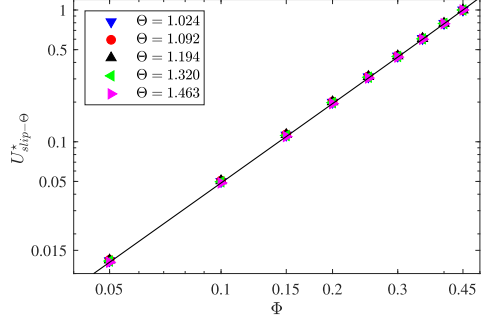
(b) Scaled velocity, $U^\star_{slip-\Theta} = U^\star_{\text{slip}}/U^\star_{\text{slip}}(\Phi = 0.45)$
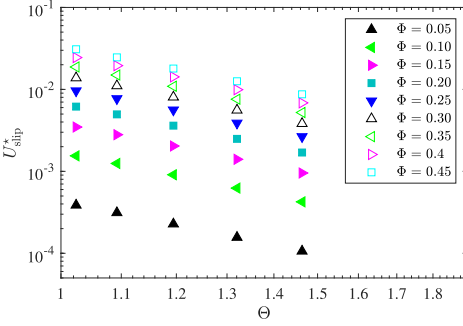
(c) Constant Porosity
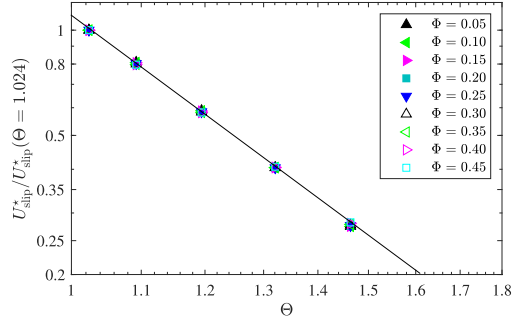
(d) Scaled velocity, $U^\star_{slip-\Phi} = U^\star_{\text{slip}}/U^\star_{\text{slip}}(\Theta = 1.024)$

FIG. 6. Slip velocity variation in terms of the porosity and tortuosity of the domain: Pressure driven flow case.

lost for all cases, when $\Theta \approx 1.5L$ and for different values of Φ, which results in a remarkable performance decrease.

For the SDF, variations of the normalized slip velocity in terms of the geometric characteristics are similar to that obtained for the PDF. Nonetheless, larger slip velocities are obtained for SDF in comparison to the PDF case. Table I indicates that the slip velocity ratio, defined as $U^\star_{\text{slip}}(\text{SDF})/U^\star_{\text{slip}}(\text{PDF})$, essentially varies linearly with both the tortuosity and the porosity. The comparison is performed for different values of tortuosity and at lowest and highest values of Φ. A factor of 35 between the slip velocity for the two flow scenarios is obtained at $\Phi = 0.05$ and $\Theta = 1.463$. These findings emphasize the important contribution of shear to the global slip velocity. This contribution is at its highest for the lowest values of void percentage.

TABLE I. Slip-velocity ratio $U^\star_{\text{slip}}(\text{SDF})/U^\star_{\text{slip}}(\text{PDF})$ between the SDF case and the PDF case. Columns represent constant Θ. Rows represent constant Φ.

	$\Theta = 1.024$	$\Theta = 1.092$	$\Theta = 1.194$	$\Theta = 1.320$	$\Theta = 1.463$
$\Phi = 0.05$	22.875	24.255	27.188	31.906	35.649
$\Phi = 0.45$	3.726	4.113	4.726	5.565	6.608

(a) Constant tortuosity, $U^{\star}_{\text{slip}} = U_{\text{slip}}/U_{\infty}$

(b) Scaled velocity, $U^{\star}_{slip-\Theta} = U^{\star}_{\text{slip}}/U^{\star}_{\text{slip}}(\Phi = 0.45)$

(c) Constant Porosity, $U^{\star}_{\text{slip}} = U_{\text{slip}}/U_{\infty}$

(d) Scaled velocity, $U^{\star}_{slip-\Phi} = U^{\star}_{\text{slip}}/U^{\star}_{\text{slip}}(\Theta = 1.024)$
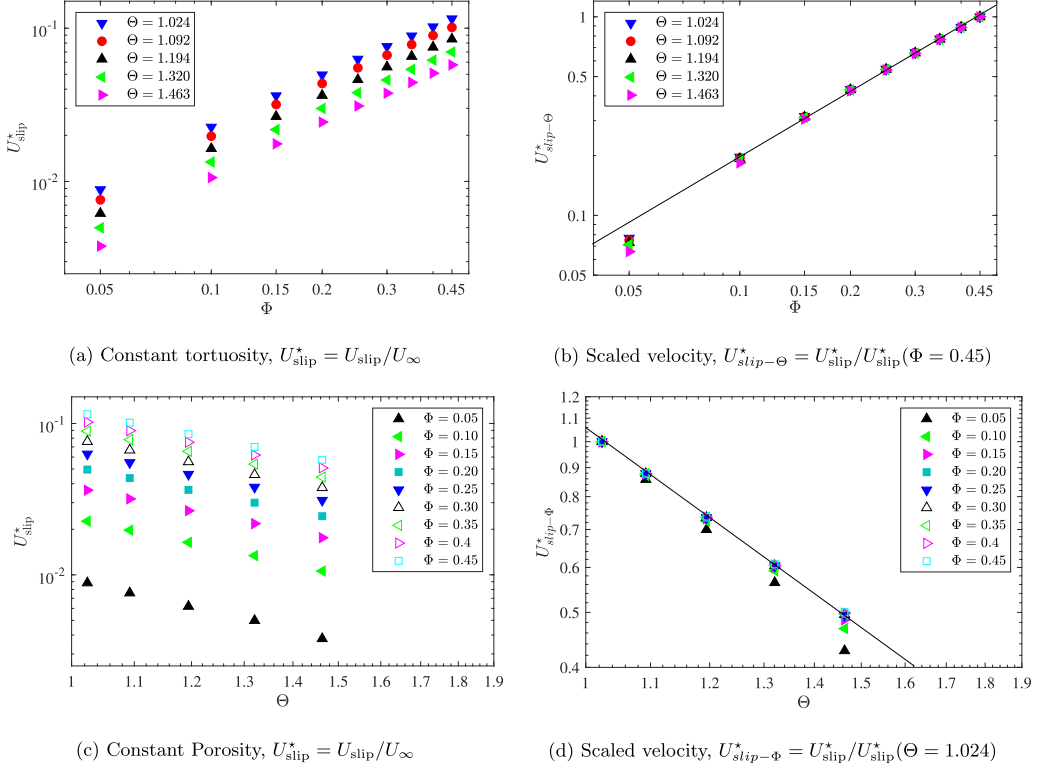
FIG. 7. Slip velocity variation in terms of the porosity and tortuosity of the domain: Shear driven flow case.

From Figs. 6(b) and 6(d) and Figs. 7(b) and 7(d), it is clear that the slip velocity scales as power laws with the tortuosity Θ and the porosity Φ of the domain such that

$$U^{\star}_{\text{slip}-} \approx C\Theta^{a}\Phi^{b}, \tag{17}$$

where C, a, and b are constants obtained from the functional relationships extracted from the numerical results for both types of flows.

The values of the constants for the two scenarios are reported in Table II. Using the linear properties of Stokes' flow for both the shear-driven flow and the pressure-driven flow, the expression of the total normalized slip velocity becomes

$$U^{\star}_{\text{slip}} = U^{\star}_{\text{slip-SDF}} + U^{\star}_{\text{slip-PDF}}. \tag{18}$$

The obtained expression can be directly applied to obtain an average value of the slip velocity given that both Φ and Θ are known. Once calculated, $U^{\star}_{\text{slip}} = U_{\text{slip}}/U_{\infty}$ can be implemented in the theoretical expression of the drag coefficient [Eq. (13)] to predict drag on a SH sphere with known porosity and tortuosity.

TABLE II. Power-law constants obtained from numerical simulations.

	C	a	b
Pressure driven flow	0.15	−3.6	2
Shear driven flow	0.32	−2	1.2

TABLE III. Comparison of correction factor from the theory of McHale *et al.* [4] and the present model. ξ_{SH} denotes the correction factor of drag on SH spheres using the present model for $\Theta = 1$ and $\Phi = 1$. $\xi_{SH\text{-}MH}$ is the counterpart computed using the theoretical model of McHale *et al.* [4].

SH-1			SH-2			SH-3		
Re_∞	ξ_{SH}	$\xi_{SH\text{-}MH}$	Re_∞	ξ_{SH}	$\xi_{SH\text{-}MH}$	Re_∞	ξ_{SH}	$\xi_{SH\text{-}MH}$
0.375		0.673	0.398		0.685	0.388		0.701
1.443	0.687	0.671	1.354	0.687	0.679	1.423	0.687	0.689
2.702		0.671	2.545		0.676	2.722		0.684

As indicated in Eq. (13), the correction factor in the current study is a function of the slip velocity on the air/liquid interface. The correction term is an implicit function of both porosity and tortuosity of the plastron. Section II A reveals that for a perfect slip condition, the slip velocity is half the value of the free stream velocity $U_{slip} = U_\infty/2$. Accordingly, the drag-correction factor from the present theoretical model would be equal to $\xi_{SH} = 2/3$. The predicted value is in good agreement with that computed using the theory of McHale *et al.* [4]. Table III confirms that the present theoretical model warrants approximately the same value of the correction factor from the model of McHale *et al.* [4].

The same conclusion can be made for the numerically correlated value for the slip velocity. For perfect slip conditions, both Φ and Θ would be equal to unity. Accordingly, the numerically computed slip would be $U_{slip} = 0.47U_\infty$, which results in an $\approx 6\%$ estimation error compared to $U_\infty/2$. Furthermore, the correlated slip velocity for a perfect plastron would result in a drag correction factor $\xi_{SH} = 0.687$.

In what follows, the drag of falling SH spheres at low Reynolds numbers is investigated experimentally. The aptitude towards drag reduction of SH spheres with randomly distributed roughness elements is first investigated. A comparison between the predicted drag on these spheres using the proposed model and the experiments follows. An additional sphere with carefully designed SH texture is later proposed, with the aim to lower Θ while keeping Φ within the same range.

III. EXPERIMENTAL SETUP

Apart from the working fluid, the experimental setup used in this study is identical to the one described in detail in Refs. [16,17]. Falling sphere experiments were performed in a transparent tank (100×100 mm^2 square cross section and 650 mm height) filled with glycerine (see Fig. 8).

All tests were performed at room temperature equal to $20 \pm 1\,^\circ$C, which was verified by a thermocouple dipped in the glycerine. The glycerine density ρ_l and dynamic viscosity μ_l were evaluated using the empirical formula proposed by Cheng [28]. The value $\mu_l = 1.41$ Pa s valid for pure glycerine at 20 $^\circ$C was further experimentally verified with a Fungilab^{TM} viscometer. At the beginning of the test, an electromagnetic holder was used to gently dip the spheres below the glycerine surface in order to assure a null velocity at release time. Stainless steel spheres with nominal diameters d equal to 5, 8, and 10 mm were taken as reference spheres. The trajectory of the falling sphere was recorded by a Phantom V341 high-speed camera at a 2560×1100 px^2 resolution, resulting in a conversion factor of 0.3 mm px^{-1}.

The recording frame rate was adapted to the sphere falling velocity, ranging from 200 fps for the $d = 5$ mm spheres up to 800 fps for the $d = 10$ mm spheres. An additional mirror was set at 45° with respect to the tank [see Fig. 8(b)]. The recorded images allowed for recovering the three-dimensional (3D) position of the sphere. The postprocessing of the recorded videos, which enabled the reconstruction of the 3D displacement of the falling sphere, was performed with the commercial software MATLAB. A cross-correlation code able to achieve subpixel accuracy by means of a Gaussian fit of the correlation peak [29] was developed. The accuracy was estimated to be approximately ± 0.06 px, which is lower than 0.4% of the smallest investigated diameter. It was
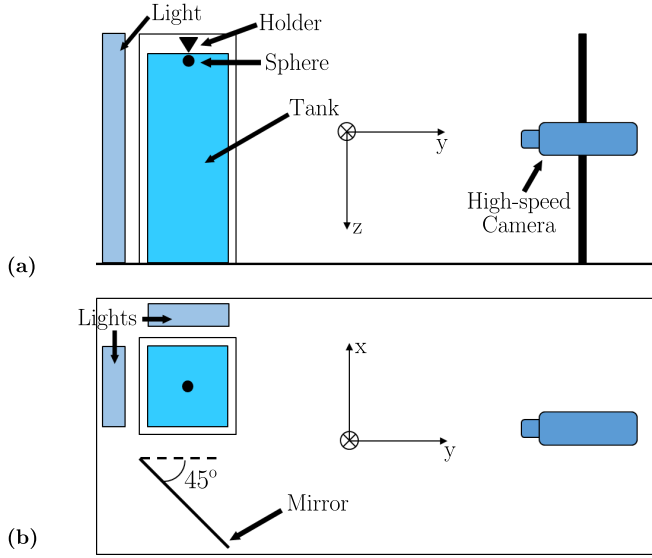
FIG. 8. The falling sphere experimental setup: (a) side view, (b) top view.

found that the sphere motion in the transverse plane (x-y) is negligible, indicating the absence of lift. Therefore, in the remainder of the paper, we only focus on vertical motion, hence drag.

Terminal velocities U_∞ were evaluated in the range 0.07–0.23 m/s, which corresponds to a terminal Reynolds number ($\mathrm{Re}_\infty = \rho_l U_\infty d / \mu_l$) lying within 0.3–2.5. Confinement effects induced by the finite size of the test section were compensated for following the technique proposed by Di Felice [30]:

$$\frac{U_\infty^{\mathrm{bou}}}{U_\infty^{\mathrm{unb}}} = \left(\frac{1 - \delta}{1 - 0.33\delta} \right)^\alpha, \tag{19}$$

where the ratio of the bounded terminal velocity U_∞^{bou} with respect to the unbounded U_∞^{unb} counterpart depends on the blockage factor $\delta = d / D_{\mathrm{tank}}^{\mathrm{eq}}$. In the latter expression, $D_{\mathrm{tank}}^{\mathrm{eq}} = 2W/\sqrt{\pi}$ (W being the tank width) is the equivalent diameter of the tank. In this study, the blockage factor δ is lower than 0.09. Finally, the exponent α in Eq. (19) was evaluated by the following expression [30]:

$$\frac{3.3 - \alpha}{\alpha - 0.85} = 0.27 \, \mathrm{Re}_\infty^{0.64}. \tag{20}$$

As explained in Ref. [17], SH coatings were produced by a spray method technique suitable for macroscopic applications using a commercially available SH paint (Ultra-Ever Dry®). Two different types of surface texturing were employed to evidence the effect of the spatial distribution of roughness on drag. The random distribution of the baseline SH coating (SH-1, no added powder) was enhanced by depositing an intermediate layer made of a carbon-based powder. Two different grades were used, and the corresponding coatings will be indicated hereafter as SH-2 (fine grain) and SH-3 (coarse grain) in order of increasing root-mean-square surface roughness λ values. The latter were evaluated by 3D confocal microscopy measurements over SH flat plates (see Fig. 2), with values in the range 25–142 μm (see Table IV).

Contact angle measurements were performed with a digital goniometer via the sessile drop technique. Glycerine drops with a volume of 6 μL were deposited over SH horizontal flat plates providing static contact angles (θ_s) in the range 137–156 deg. The highest θ_s was obtained with the SH-1 coating, while a λ increase determined a θ_s reduction, in good agreement with the findings reported in Ref. [31] for surface roughness in the same range of our study. The same approach was

TABLE IV. Properties of the manufactured SH coatings. λ, root-mean-square surface roughness. θ_s, static contact angle. θ_r, roll-off angle. θ_h, hysteresis angle. h_r, horizontal size of the roughness elements. h_s, horizontal spacing of the roughness elements. Φ_{LA}, gas fraction. The reported uncertainties represent the 95% confidence level. The missing values in the SH-1 coating are not reported since they are considered not reliable, due to limitations of the adopted technique.

	SH-1	SH-2	SH-3
λ (μm)	25 ± 4	74 ± 12	142 ± 23
θ_s (deg)	156.4 ± 5.8	147.3 ± 7.6	136.7 ± 12.0
θ_r (deg)	2.6 ± 0.8	2.3 ± 0.8	5.4 ± 2.6
θ_h (deg)	4.9 ± 3.1	5.5 ± 3.9	11.6 ± 4.9
h_r (μm)		77 ± 12	183 ± 96
h_s (μm)		116 ± 48	209 ± 99
Φ_{LA}	0.59 ± 0.06	0.54 ± 0.06	0.55 ± 0.05

followed to evaluate the roll-off (θ_r) and the hysteresis (θ_h) angles by tilting the SH flat plates at a controlled rate of 0.5 deg/s. The roll-off angle (θ_r), which was considered in this study as the lowest tilt angle that caused the drop to roll off, reached the highest value of 5.4 deg in the SH-3 case, whereas a λ decrease determined a θ_r reduction down to 2.6 deg for the SH-1 coating. The hysteresis angle (θ_h), defined as the difference between the advancing and receding angles at the time instant where the drop starts to roll off [32], reached the highest value of 11.6 deg in the SH-3 case, while it decreased down to 4.9 deg for the SH-1 coating with the lowest λ. The SH coatings determined a d increase (measurement accuracy 10 μm) with respect to the reference spheres, with a maximum +10% in the SH-3 case. The masses of the reference spheres (measurement accuracy 0.1 mg) were 0.51, 2.07, and 4.04 g for the spheres with diameter 5, 8, and 10 mm, respectively. The SH coatings determined a mass increase up to +6% in the SH-3 case. Full details of the experimental setup, SH coatings manufacturing procedure, sphere properties, and postprocessing techniques can be found in [17]. It is worth noting that the spheres recovered after the falling experiment were dry, which confirms that the air layer is present all the way during the drop of the sphere in the tank (see Fig. 9). The glycerine-filled tank was tall enough to allow every sphere to reach its respective terminal velocity U_∞.
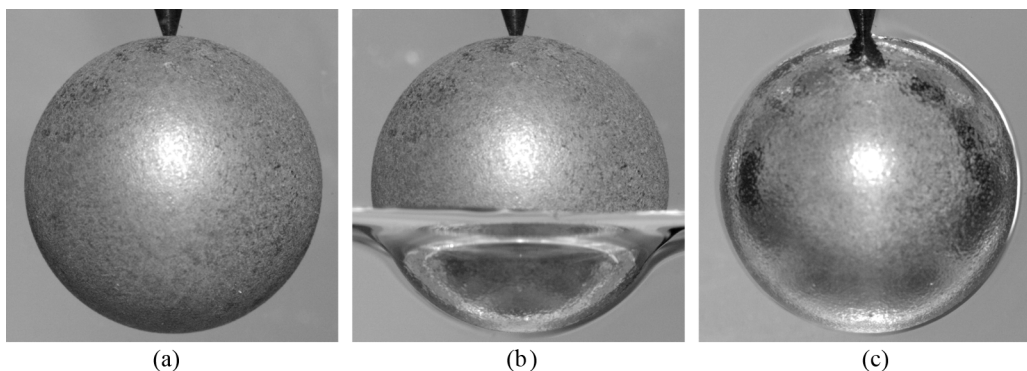

(a)   (b)   (c)

FIG. 9. Visual evidence of the air layer around a superhydrophobic sphere (SH-1 coating, $d = 15$ mm diam) progressively dipped in glycerine. (a) Air, (b) partially dipped, and (c) fully immersed. Image (b) underlines the difference between the area above the glycerine surface and the part of the sphere dipped in the glycerine. The bright appearance in images (b) and (c) testifies to the establishment of the air layer. The thickness of the air layer is qualitatively discernible in both images (b) and (c).

TABLE V. Nondimensional characteristic times for the different physical mechanisms at stake during the experiments. $Ca_D = \mu_l U_D/\gamma$ denotes the capillary number where $U_D = \sqrt{(\zeta - 1)gd}$ is chosen as the scaling velocity in order to account for gravity/buoyancy effects [33] and the Reynolds number Re_D is defined accordingly, Ma denotes the Marangoni number, and ν denotes the kinematic viscosity.

	$t_C^\star \approx \sqrt{Re_D Ca_D}$	$t_M^\star \approx \pi Ma^{-1}$	$t_P^\star \approx (\frac{\lambda}{2R})^2 Re_D \frac{\nu_l}{\nu_a}$
SH-1	~ 10	$\sim 6.4 \times 10^2$	$\sim 3 \times 10^{-3}$
SH-2	~ 9.6	$\sim 6.2 \times 10^2$	$\sim 2.4 \times 10^{-2}$
SH-3	~ 9.2	$\sim 5.9 \times 10^2$	$\sim 8.7 \times 10^{-2}$

As indicated previously, various mechanisms may be responsible for the loss of the performances of SH spheres compared to their no-slip counterparts. To verify the relevance/irrelevance of these mechanisms with respect to the free-fall time, a timescale analysis is conducted. Capillary-induced deformation, Marangoni stresses, and air resistance through the plastron are considered. The time characteristic scale for each mechanism is provided in detail in the Supplemental Material [26], and Table V summarizes the different timescales for the present experiment. It is found that the characteristic timescales for both the Marangoni effect and interface deformation are very large in comparison with the influence of the texture on the flow. These results further confirm the assumption that air motion through the plastron has an important effect on the slip velocity.

IV. RESULTS AND DISCUSSIONS

A. Randomly distributed roughness elements

Drag for SH surfaces with randomly distributed roughness elements was first investigated and compared to the theoretical Stokes drag and that obtained using an experimental correlation [34]:

$$C_{D\text{-ST}} = \frac{24}{Re_\infty}, \tag{21}$$

$$C_{D\text{-NS}} = \frac{24}{Re_\infty} \left(1 + 0.15 \, Re_\infty^{0.687}\right). \tag{22}$$

The subscript $-$NS refers to the no-slip case. The terminal drag coefficient in the experimental case was computed using the following relation for the different SH spheres:

$$C_{D\text{-Exp}} = 4dg(\zeta - 1)/\left(3U_\infty^2\right), \tag{23}$$

where g is the acceleration due to gravity, and $\zeta = \rho_s/\rho_l$ is the density ratio between the metal of the sphere and the glycerine, in the range 4.8–6.1.

Figure 10 shows the terminal drag coefficient $C_{D\infty}$ as a function of Re_∞ for the spheres analyzed in this study. The performance of each SH sphere is quantified as a function of Re_∞. The evaluation is performed using the no-slip sphere as a reference. Stokes' formula and the experimental correlation presented above are used as the reference drag, and drag-reduction performance is evaluated as follows:

$$\Delta C_{D\text{-NS}} = 1 - \frac{C_{D\text{-Exp}}}{C_{D\text{-NS}}}. \tag{24}$$

Results for different values of Re_∞ are reported in Table VI. A first glance at Fig. 10 indicates that SH coatings investigated in the current study presented a slight drag reduction in comparison to the experimental correlation. For instance, at low Re_∞ (i.e., <0.4), there is no significant evidence of drag reduction in the case of randomly distributed SH coatings. In actual fact, Fig. 10 further indicates that when compared to Stokes drag, SH-1 coating resulted in a slight increase of drag. Quite the opposite, when compared to the correlated drag, it is found that the differently coated
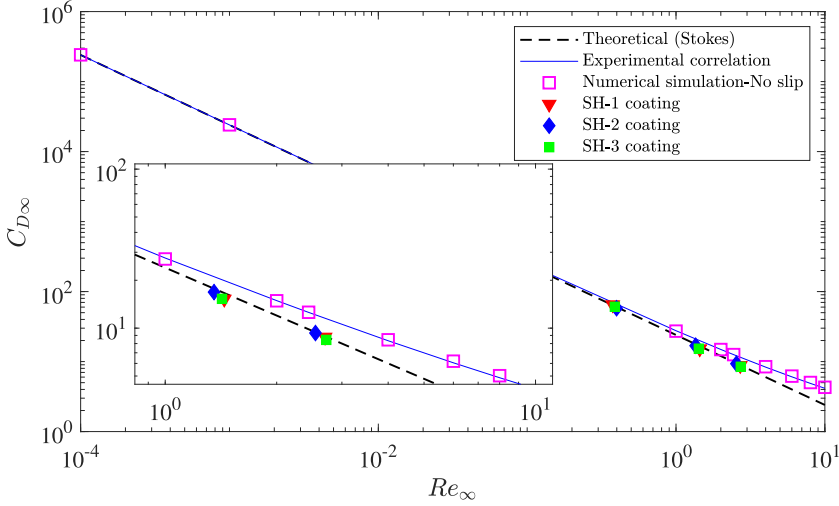
FIG. 10. Terminal drag coefficient $C_{D\infty}$ as a function of the terminal Reynolds number Re_∞. ▼, SH-1 coating. ◆, SH-2 coating. ■, SH-3 coating. The error bars (95% confidence level) are of the same order as the size of the symbols. The dashed line shows Stokes' law ($C_{D\infty} = 24/Re_\infty$).

spheres did modify the features of the flow. The drag reduction performance $\Delta C_{D\text{-NS}}$ ranges from 5.7% to 11%. Note that the reported negligible drag reduction is always in agreement with the findings of Ahmmed *et al.* [11].

At Re > 1, SH effects become more pronounced and a drag reduction of $\Delta C_{D\text{-ST}} \approx 22\%$ is reported for all experiments. As a matter of fact, the drag reduction increases with increasing value of Re_∞. For instance, the SH-3 coating resulted in a drag reduction up to 26.3% ($Re_\infty = 2.722$). The mild performance of drag reduction is still in the range of maximum performance predicted by analytical studies and numerical simulations [4,9]. In the case of perfect plastron, McHale *et al.* [4] provided an expression to compute drag for SH surfaces as a function of the thickness of the plastron. It has been shown that when an optimum plastron thickness can be achieved, drag reduction can approach 20–30%. This comparison may not be valid since the features of the plastron from the current study cannot be considered as perfect air layer conditions due to the presence of roughness elements. Additionally, it should be noted that no considerable effect of the surface roughness size can be derived, since the error bars (95% confidence level) of the different coatings tend to overlap.

These findings emphasize the limited performance of SH surfaces with randomly distributed roughness elements of producing significant drag reduction at low Re flow. For instance, at the very lowest value of Re, for the three different coatings, the experimentally measured drag was found to be larger than that predicted by the Stokes formula. Nevertheless, it remains smaller than that computed using the experimental correlation.

TABLE VI. Variation of the terminal drag coefficient $\Delta C_{D\infty}(\%)$ of the SH spheres with respect to the corresponding reference sphere, as a function of the terminal Reynolds number Re_∞.

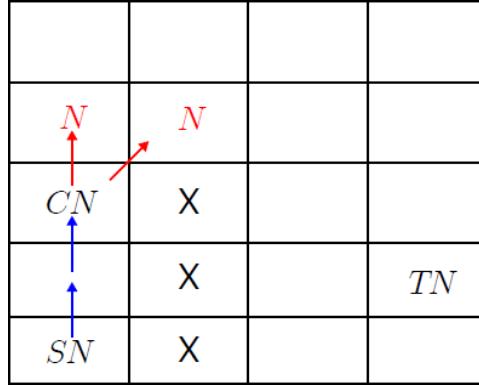| SH-1		SH-2		SH-3	
Re_∞	$\Delta C_{D\infty}$	Re_∞	$\Delta C_{D\infty}$	Re_∞	$\Delta C_{D\infty}$
0.375	5.70	0.398	11	0.388	8.94
1.443	23.25	1.354	19.72	1.423	23.89
2.702	23.76	2.545	23.10	2.722	26.30

FIG. 11. Schematic of the $A^{\star}$ algorithm principles. The optimal path from the starting node SN to the target node TN is sought, taking into account the presence of the obstacles X. The next node N is selected from the current node.

The next step aims at comparing the drag obtained experimentally for various SH spheres with that predicted using the homogenized model. To determine the homogenized BC for the different coatings, values of the porosity and geometric tortuosity are required. For the randomly distributed roughness spheres, the porosity for each coating type is reported in Table IV. To estimate the actual value of Θ for a given coating, 3D confocal microscopy images were analyzed. Images were binarized setting a threshold equal to the rms roughness height λ. Then, an A^* path detection algorithm from a starting node SN to a target node TN was implemented [35]. The basic principles of the code are resumed by the schematic in Fig. 11. For each current node CN, the algorithm minimizes the cost function $f(N)$ to select the following node N:

$$f(N) = g(N) + h(N), \tag{25}$$

where $g(N)$ is the cost based on the distance from N to TN and $h(N)$ is the cost based on the distance from CN to N. The optimal path is therefore progressively evaluated from SN to TN.

The output of this algorithm applied to the actual SH coatings microscope images is reported in Fig. 12, where the case of the SH-2 coating is taken as an example. The value $\Theta = 1.6$ is estimated in the optimal path case in Fig. 12(a). However, by artificially forcing the code to follow nonoptimal paths, the tortuosity value can quickly be increased. For example, the value $\Theta = 3.2$ is retrieved in Fig. 12(b). This shows that a precise and statistically relevant Θ estimation from the available information on the produced SH coatings is not straightforward. In fact, the $A^{\star}$ algorithm applied to the other SH coatings provided the same Θ order of magnitude. It is worth noting that this range
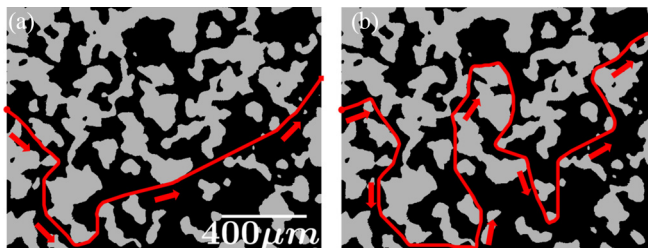

FIG. 12. Path detection on a binarized 3D confocal image of a SH-2 coating flat plate. (a) Optimal path, (b) nonoptimal path. The black and gray regions indicate the areas below and above the rms surface roughness λ, respectively. The red dot and square indicate the starting and target points, respectively. The red arrows indicate the path direction.

TABLE VII. Summary of computed drag: theoretical, experimental, and numerical. Re_∞, Reynolds number. $C_{D\text{-NC}}$, drag coefficient using the correlation. $C_{D\text{-Exp}}$, experimental drag coefficient. $C_{D\text{-SH}}$, computed drag coefficient using the present model.

	Re_∞	$C_{D\text{-NS}}$	$C_{D\text{-Exp}}$	Φ	Θ	$\frac{U_{\text{slip}}}{U_\infty}$	$C_{D\text{-SH}}$	Error (%)	Θ	$\frac{U_{\text{slip}}}{U_\infty}$	$C_{D\text{-SH}}$	Error (%)
	0.375	68.759	64.840				60.7	6.384			63.152	2.600
SH-1	1.443	19.831	15.220	0.59		0.074	15.798	−3.800		0.016	16.436	−8
	2.702	11.519	8.782				8.441	3.884			8.782	0.002
	0.398	64.987	57.832				57.520	0.539			59.579	−3.020
SH-2	1.354	20.989	16.849	0.54	1.6	0.066	16.930	−0.484	3.2	0.015	17.536	−4.081
	2.545	12.116	9.317				9.011	3.285			9.334	−0.175
	0.388	66.645	60.684				59.002	2.772			61.167	−0.795
SH-3	1.423	20.083	15.286	0.55		0.068	16.095	−5.294		0.015	16.685	−9.157
	2.722	11.446	8.436				8.415	0.245			8.724	−3.414

corresponds to the typical empirical values reported in the literature (see Ref. [36], and references therein).

Since exact data for the tortuosity are not available, obtained values from the above described algorithm were used as limiting cases for Θ. Consequently, drag was computed using two extreme values of Θ for SH spheres with randomly distributed elements ($\Theta = 1.6$ and 3.2). Obtained results, therefore, represent a maximum and minimum computed drag using the model.

Table VII summarizes the results of the computed drag for the different SH spheres. At first glance, the proposed model provides a good estimation of drag on SH surfaces. Predicted values for the various coatings were in good agreement with experiments. The relative error for the model predictions was found to be less than approximately 9%. Note that the normalized slip velocity at $\Theta = 1.6$ is greater than the value calculated at $\Theta = 3.2$. These results demonstrate that high values of the tortuosity contribute to decreasing SH performances. The drag predicted by the model for spheres SH-1, SH-2, and SH-3 is compared to their experimental counterparts in Fig. 13. Overall, the range of the predicted drag overlaps very well with the error bars from the experiments. It is assumed that the small disparity in the results stems from the inexact estimation of Θ.

These findings emphasize the need for shorter paths for air inside the plastron such that SH surfaces may achieve a significant drag reduction. More precisely, the air path should be approximately straight to achieve the least resistance as air flows inside the plastron. To validate this assumption, an additional SH sphere was manufactured to investigate the effect of regularly distributed roughness elements on drag decrease.

B. Regularly distributed roughness sphere

Figure 14 depicts a schematic of a CV with cylindrical pillars as roughness elements. Since the pillars are structurally distributed over the surface, the air flows approximately straight ($L_\Theta \approx L$). Using this concept, a SH sphere textured with a regular distribution of pillars (SH-RDR) was 3D-printed (only for the $d = 10$ mm case) to assess experimentally the impact of roughness alignment on drag. Figure 14 also shows a 3D rendering of the model used to 3D-print an empty shell which hosts a $d = 10$ mm reference stainless steel sphere. The surface roughness is characterized by aligned and equidistant cylindrical pillars with $\lambda \approx 75$ μm. The distance between pillars was also kept in the same range, once the SH coating was applied. A qualitative assessment of the presence of the air-layer around the SH sphere dipped in pure glycerine was performed to make sure that the air layer was well present. The result is presented in Fig. 14 (3D-printed SH sphere).

Table VIII summarizes the result for the 3D-printed sphere with regular grooves and equally spaced pillars. SH-RDR shows an interesting drag reduction improvement with a mean reduction of approximately 31% with respect to the reference sphere. This outstanding performance can be
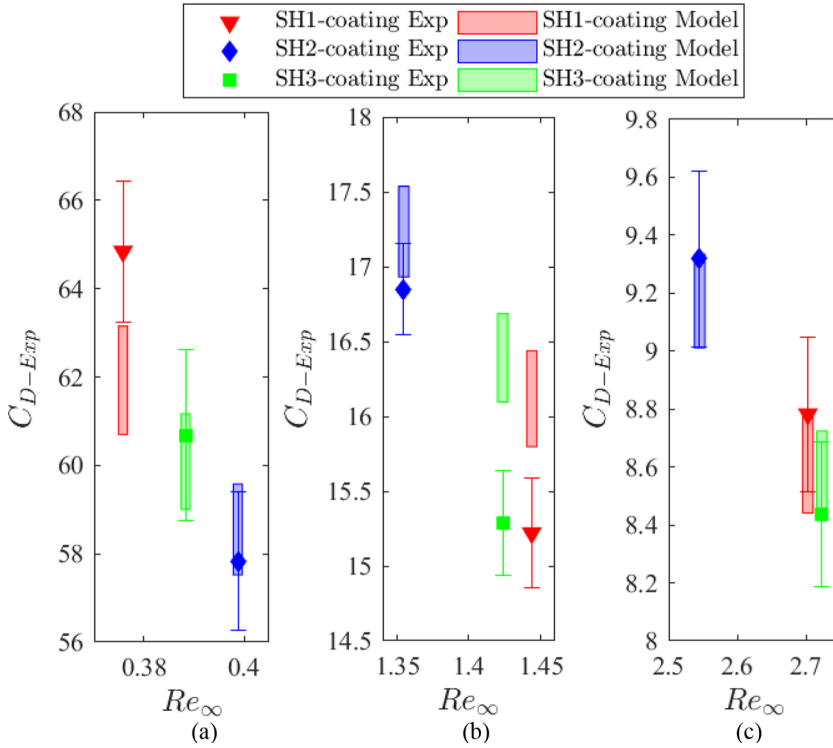
FIG. 13. Comparison between the obtained experimental drag and the value calculated using the developed model. (a) Reynolds number $Re_{\infty-1}$. (b) Reynolds number $Re_{\infty-2}$. (c) Reynolds number $Re_{\infty-3}$. ▼, SH-1 coating. ◆, SH-2 coating. ■, SH-3 coating. █ predicted drag range for SH1, █ predicted drag range for SH2, █ predicted drag range for SH3.

explained by the fact that with pillars, the tortuosity is minimized and independent of the orientation of the sphere during its fall. This result highlights the potential role of a regular surface texture in improving drag reduction.

For the 3D-printed sphere with cylindrical pillars, a relatively exact value of Θ can be calculated. The CAD model of the SH-RDR sphere was designed to display a final SH coating whose elements
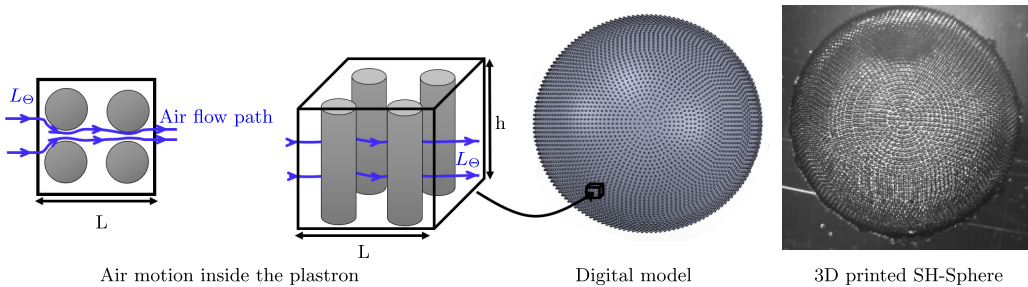

FIG. 14. Schematic of a porous medium model over a CV (length L and height h) inside the air layer on the surface of a SH sphere with regularly distributed pillars. The digital model of the regularly distributed roughness SH sphere was manufactured by 3D printing. Note the minimization of the tortuosity throughout the regularly distributed roughness elements.

TABLE VIII. Summary of computed drag coefficient, theoretically, experimentally, and numerically for the regularly distributed roughness sphere SH-RDR. $C_{D\text{-NS}}$, correlation drag coefficient. $C_{D\text{-Exp}}$, experimental drag coefficient. $C_{D\text{-SH}}$, computed drag coefficient using the present model.

	Re_∞	$C_{D\text{-NS}}$	$C_{D\text{-Exp}}$	Φ	Θ	$\dfrac{U_{\text{slip}}}{U_\infty}$	$C_{D\text{-SH}}$	Error (%)
SH-RDR	2.439	12.562	8.708	0.65	1.087	0.206	8.483	2.589

spacing and size were comparable to the randomly distributed SH coatings described in the previous subsection. The regular imposed geometry also allowed an estimation of the void fraction with respect to the total volume providing a porosity $\Phi = 0.65$. Going back to Fig. 14, the SH-coated sphere presents a relative alignment of the printed roughness elements with respect to the digital model. Consequently, the tortuosity would be slightly larger but yet very close to unity, $\Theta \gtrsim 1$. It is therefore assumed that the air motion follows a sinuous path around the pillars with an amplitude equal to half the distance between the center of the pillars. In this case, an approximate tortuosity for the SH-RDR would be $\Theta = 1.087$. Table VIII further indicates that predicted drag for the SH-RDR sphere, which provides the best estimation of Θ, is in very good agreement with the experimental value. An estimation error of 2.589% was obtained. Therefore, provided with exact values of Φ and Θ, the present model appears to be capable of predicting accurate values of drag for SH surfaces.

The efficiency of the different SH coatings is further scrutinized using the following expression:

$$\eta_{C_D} = \frac{C_{D\text{-NS}} - C_{D\text{-Exp}}}{C_{D\text{-NS}} - C_{D\text{-FS}}}. \tag{26}$$

The previous expression scales $\eta C_{D\infty}$ between zero for the no-slip case and unity for a sphere with the free-slip (FS) condition at the wall. Figure 15 indicates that the only sphere that provided drag close to that obtained with a free-slip condition was the SH-RDR model, whose tortuosity is minimized and its efficiency is 82%. In other words, controlling the geometric properties of a SH surface may result in hydrodynamic performances close to that of a free-slip condition. These
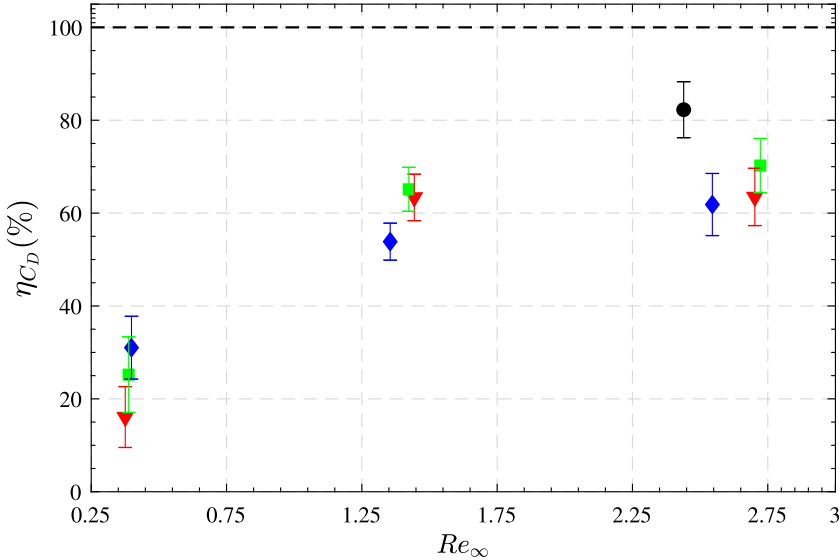

FIG. 15. η_{C_D} as a function of the terminal Reynolds number Re_∞. ▼, SH-1 coating. ◆, SH-2 coating. ■, SH-3 coating. ●, regular roughness SH coating. The error bars (95% confidence level) are of the same order as the size of the symbols. The dashed line outlines the optimum performance, where $C_{D\text{-Exp}} = C_{D\text{-FS}}$.

findings further support the homogenization approach as a viable way to design and predict the performances of SH textures in the laminar regime.

V. CONCLUSIONS

An approach is introduced to elucidate the slip-reduction performances of SH surfaces at low Reynolds number where the slippery effects are found to be ascribed to the motion of entrapped air inside the surface roughness elements. This coupled fluid problem is tackled using a homogenization approach coupling an analytical solution for the creeping flow of a liquid around a sphere and the flow of air inside complex groovy surfaces. The model is finally tested and validated against laboratory experiments with an excellent agreement.

One of the key contributions of this work is the identification of parameters that play an important role in the performances of SH surfaces. The lubricating effect of SH surfaces is analyzed using a porous medium approach characterized by two control parameters: porosity and tortuosity. While the effect of porosity was already studied in the past [21], the effect of tortuosity is the focus of the present study. Numerical simulations were conducted in order to compute the air flow inside the textured surface, and the mean slip velocity was found to scale as power laws as a function of both the porosity and the tortuosity. These scaling laws are then used to homogenize the boundary condition for the slip velocity. The developed expressions demonstrate that the tortuosity of the domain should be minimized in order to obtain significant drag reduction. Simultaneously, the porosity of the roughness elements should remain as high as possible but should also ensure the stability of the air layer (i.e., sufficiently large contact angles). The homogenized boundary condition was later implemented in the analytical model to predict drag of SH spheres manufactured using different processes.

The accuracy of the homogenized model is supported through experimental measurements of free-falling SH spheres in glycerine. Experiments were designed to highlight the particular decrease of the hydrodynamic performances of superhydrophobic surfaces due to complex surfaces with a large tortuosity. Negligible to mild drag-reducing effects are reported for various randomly distributed SH coatings at low Reynolds numbers. This comparative study between the predicted values and experiments shows that the homogenized model is capable of accurately estimating drag for superhydrophobic surfaces. This in turn requires estimating values of the porosity and tortuosity, and a method is provided.

A surface texture was later proposed to test the potential role of the surface geometric properties on drag reduction. A 3D printed sphere with regular roughness elements was manufactured for this purpose. This sphere demonstrated promising drag-reduction performances close to free-slip conditions, which confirms that tortuosity is a key parameter in improving the performances of SH coating and subsequent textures for drag-reduction applications.

To conclude, this study shows that a compromise between scalable industrial spray coating and expensive small-scale regular geometry techniques should be found in the attempt to reproduce the outstanding performance of the lotus leaves on large industrial applications (see, for instance, Ref. [37]). Finally, it must be noted that some of the conclusions proposed above could still be valid at higher Reynolds numbers, since works available in the literature (see, e.g., Ref. [38]) have shown the pivotal role of the relative viscous sublayer thickness with respect to the superhydrophobic coating features in turbulent flows.

Finally, it is worthwhile to highlight that the present model does not predict the evolution of the ratio between the detrimental surface roughness resistance and the beneficial slip lubricating at high Reynolds number, which is left to future work.

[1] G. G. Stokes, On the effect of the internal friction of fluids on the motion of pendulums, Trans. Cambridge Philos. Soc. **IX**, 8 (1851).

[2] A. M. Albano, D. Bedeaux, and P. Mazur, On the motion of a sphere with arbitrary slip in a viscous incompressible fluid, Physica A **80**, 89 (1975).

[3] D. Quéré, Wetting and roughness, Annu. Rev. Mater. Res. **38**, 71 (2008).

[4] G. McHale, M. R. Flynn, and M. I. Newton, Plastron induced drag reduction and increased slip on a superhydrophobic sphere, Soft Matter **7**, 10100 (2011).

[5] S. L. Ceccio, Friction drag reduction of external flows with bubble and gas injection, Annu. Rev. Fluid Mech. **42**, 183 (2010).

[6] I. U. Vakarelski, J. O. Marston, D. Y. C. Chan, and S. T. Thoroddsen, Drag Reduction by Leidenfrost Vapor Layers, Phys. Rev. Lett. **106**, 214501 (2011).

[7] O. I. Vinogradova, Slippage of water over hydrophobic surfaces, Int. J. Miner. Proc. **56**, 31 (1999).

[8] J. P. Rothstein, Slip on superhydrophobic surfaces, Annu. Rev. Fluid Mech. **42**, 89 (2010).

[9] B. R. K. Gruncell, N. D. Sandham, and G. McHale, Simulations of laminar flow past a superhydrophobic sphere with drag reduction and separation delay, Phys. Fluids **25**, 043601 (2013).

[10] C. Byon, Y. Nam, S. J. Kim, and Y. S. Ju, Drag reduction in stokes flows over spheres with nanostructured superhydrophilic surfaces, J. Appl. Phys. **107**, 066102 (2010).

[11] K. M. T. Ahmmed, C. Patience, and A.-M. Kietzig, Internal and external flow over laser-textured superhydrophobic polytetrafluoroethylene (PTFE), ACS Appl. Mater. Interfaces **8**, 27411 (2016).

[12] C. D. Modak and S. K. Bhaumik, Creeping flow dynamics over superhydrophobic ball: Slip effects and drag reduction, Colloids Surf. A **529**, 998 (2017).

[13] F. J. Peaudecerf, J. R. Landel, R. E. Goldstein, and P. Luzzatto-Fegiz, Traces of surfactants can severely limit the drag reduction of superhydrophobic surfaces, Proc. Natl. Acad. Sci. (USA) **114**, 7254 (2017).

[14] D. Song, B. Song, H. Hu, X. Du, P. Du, C.-H. Choi, and J. P. Rothstein, Effect of a surface tension gradient on the slip flow along a superhydrophobic air-water interface, Phys. Rev. Fluids **3**, 033303 (2018).

[15] J. R. Landel, F. J. Peaudecerf, F. Temprano-Coleto, F. Gibou, R. E. Goldstein, and P. Luzzatto-Fegiz, A theory for the slip and drag of superhydrophobic surfaces with surfactant, J. Fluid Mech. **883**, A18 (2020).

[16] M. Castagna, N. Mazellier, and A. Kourta, On the onset of instability in the wake of super-hydrophobic spheres, Int. J. Heat Fluid Flow **87**, 108709 (2021).

[17] M. Castagna, N. Mazellier, and A. Kourta, Wake of super-hydrophobic falling spheres: influence of the air layer deformation, J. Fluid Mech. **850**, 646 (2018).

[18] J.-H. Kim and J. P. Rothstein, Role of interface shape on the laminar flow through an array of superhydrophobic pillars, Microfluid Nanofluid **21**, 78 (2017).

[19] R. N. Govardhan, G. S. Srinivas, A. Asthana, and M. S. Bobji, Time dependence of effective slip on textured hydrophobic surfaces, Phys. Fluids **21**, 052001 (2009).

[20] H. Ling, J. Katz, M. Fu, and M. Hultmark, Effect of reynolds number and saturation level on gas diffusion in and out of a superhydrophobic surface, Phys. Rev. Fluids **2**, 124005 (2017).

[21] C. Ybert, C. Barentin, C. Cottin-Bizonne, P. Joseph, and L. Bocquet, Achieving large slip with superhydrophobic surfaces: Scaling laws for generic geometries, Phys. Fluids **19**, 123601 (2007).

[22] S. B. Naqvi and A. Bottaro, Interfacial conditions between a free-fluid region and a porous medium, Int. J. Multiphase Flow **141**, 103585 (2021).

[23] A. Bottaro and S. B. Naqvi, Effective boundary conditions at a rough wall: A high-order homogenisation approach, Meccanica **55**, 1781 (2020).

[24] A. Premlata and H.-H. Wei, The basset problem with dynamic slip: Slip-induced memory effect and slip-stick transition, J. Fluid Mech. **866**, 431 (2019).

[25] P. Du, J. Wen, Z. Zhang, D. Song, A. Ouahsine, and H. Hu, Maintenance of air layer and drag reduction on superhydrophobic surface, Ocean Eng. **130**, 328 (2017).

[26] See Supplemental Material at http://link.aps.org/supplemental/10.1103/PhysRevFluids.7.094101 for supplemental details on the development of the theoretical and CFD models and the timescale analysis for the drag reduction mechanisms as described in the main text.

[27] H. R. T. Jinlong Fu and C. Li, Tortuosity of porous media: Image analysis and physical simulation, Earth-Sci. Rev. **212**, 103439 (2021).

[28] N.-S. Cheng, Formula for the viscosity of a glycerol-water mixture, Ind. Eng. Chem. Res. **47**, 3285 (2008).

[29] M. Raffel, C. Willert, S. Wereley, and J. Kompenhans, *Particle Image Velocimetry* (Springer, Berlin, Heidelberg, 2007).

[30] R. Di Felice, A relationship for the wall effect on the settling velocity of a sphere at any flow regime, Int. J. Multiphase Flow **22**, 527 (1996).

[31] M. A. Nilsson, R. J. Daniello, and J. P. Rothstein, A novel and inexpensive technique for creating superhydrophobic surfaces using Teflon and sandpaper, J. Phys. D **43**, 045301 (2010).

[32] L. Gao and T. J. McCarthy, Contact angle hysteresis explained, Langmuir **22**, 6234 (2006).

[33] M. Jenny, J. Dušek, and G. Bouchet, Instabilities and transition of a sphere falling or ascending freely in a newtonian fluid, J. Fluid Mech. **508**, 201 (1999).

[34] R. Clift, J. Grace, and W. Weber, *Bubbles, Drops and Darticles* (Academic Press, New York, 1978).

[35] E. S. Ueland, R. Skjetne, and A. R. Dahl, Marine autonomous exploration using a lidar and slam, in *Proceedings of the ASME 2017 36th International Conference on Ocean, Offshore and Arctic Engineering* (ASME, Trondheim, Norway, 2017), Vol. 61880.

[36] J. Bear, *Dynamics of Fluids in Porous Media* (Dover, New York, 1988).

[37] H. J. Ensikat, P. Ditsche-Kuru, C. Neinhuis, and W. Barthlott, Superhydrophobicity in perfection: The outstanding properties of the lotus leaf, Beilstein J. Nanotechnol. **2**, 152 (2011).

[38] R. J. Daniello, N. E. Waterhouse, and J. P. Rothstein, Drag reduction in turbulent flows over superhydrophobic surfaces, Phys. Fluids **21**, 085103 (2009).